The effects of stress, temperature and facet structure on growth of 1012 twins in Mg: A molecular dynamics and phase field study

Mingyu Gong, J. Graham, Vincent Taupin, Laurent Capolungo

To cite this version:

Mingyu Gong, J. Graham, Vincent Taupin, Laurent Capolungo. The effects of stress, temperature and facet structure on growth of 1012 twins in Mg: A molecular dynamics and phase field study. Acta Materialia, 2021, 208, pp.116603. 10.1016/j.actamat.2020.116603 . hal-03138713

The effects of stress, temperature and facet structure on growth of $\{10\bar{1}2\}$ twins in Mg: A molecular dynamics and phase field study

Mingyu Gong[a,b], J. Graham[b], Vincent Taupin[c], Laurent Capolungo[b,*]

[a] University of Nebraska at Lincoln, Lincoln, NE 68588, USA
[b] Materials Science and Technology Division (MST-8), Los Alamos National Laboratory, Los Alamos, NM 87545, USA
[c] Université de Lorraine, CNRS, Arts et Métiers ParisTech, LEM3, F-57000 Metz, France

ABSTRACT

The present study focuses on the roles of structure, stress and temperature on the mobility of facets bounding twin domains and on the overall impact on the growth kinetics of $\{10\bar{1}2\}$ twins in Mg. We first use molecular dynamics simulations (MD) to study the relationship between interface structures, stress, temperature and mobility. As facets can exhibit distinct atomic scale structures, we also quantify the effect of stress relaxation mediated by misfit dislocations on the mobility of the basal-prismatic interface. The information gathered for ten different facets is used to calibrate an anisotropic phase field model predicting the effects of temperature and stress on the kinetics and shape of a growing $\{10\bar{1}2\}$ 3D twin, by comparison with MD data. The comparative analysis suggests that, as compared to simulations of individual facets, the effective mobility of facets can be significantly different during growth of a 3D twin. This can be attributed to the complex three-dimensional internal stress state of the twin and to coupling in facet motion triggered by facet junctions. As such, by directly fitting both the twin growth kinetics and morphology as predicted by MD for different stresses and temperatures, we can identify a limited set of rate-limiting facets that control twin growth and morphology, and measure their effective mobility.

1. Introduction

Deformation twins can be readily activated in hexagonal closed packed (hcp) media to accommodate plastic deformation along the c-axis of the host crystals [1,2]. Historically, a large number of fundamental studies on twinning in hcp metals have focused on $\{10\bar{1}2\}$ twinning in Mg owing to its elastic properties (i.e. minimal elastic anisotropy) and potential industrial applications. A microstructure deformed by deformation twins will likely contain a relatively complex network of 3-dimensional twin domains for which the shape, while often idealized as ellipsoidal, can adopt particularly irregular morphologies (e.g. concave shapes, large fluctuations in thickness for a given twin, etc.) [3–8]. This has been shown by serial section of deformation samples and use of electron back scattering diffraction (EBSD) to reconstruct 3-dimensional twinned volumes [7]. The complex 3-dimensional twin shapes result from (i) the local fluctuations in internal stresses (providing non-uniform driving forces for growth) [9–11], (ii) the potential anisotropy in the migration mode of defects mediating the twin transformation [4,9,12] and (iii) the short-range interactions between twin domains and other defects (i.e. grain boundaries, twins, dislocations, precipitates) [13–16]. Naturally, a rigorous understanding of the relative contribution of these effects necessitates that the defects and facets which bound twin domains and carry the twin transformation be fully characterized. In this regard, a relatively large body of work has been dedicated to studying admissible defects and facets connected to the coherent twin boundary [6,17–25]. These 2-dimensional studies offer a partial rendering of the large panoply of energetically favorable defects and facets that can bound a 3-dimensional twin domain [5,8,26–28].

Recently, studies using high resolution transmission electron microscopy (HRTEM) [3,8] and MD simulations [5,6,26,28] have yielded a comprehensive 3-dimensional picture of the types and geometry of facets that can bound a 3D $\{10\bar{1}2\}$ twin in Mg. For instance, in addition to the $\{10\bar{1}2\}$ coherent twin boundary (CTB) [29–31], other interfaces, such as basal-prismatic or prismatic-basal (BP, PB) interfaces [18,19,21,22,24,25,32–34] in the twinning direction, twist pyramidal-pyramidal and twist prismatic-prismatic (Twist-PyPy1, Twist-PrPr2) facets [3,8,17,26,27] in the transverse direction, or tilt pyramidal-pyramidal (Tilt-PyPy1) facets [8] in an intermediate direction, were reported. To understand the kinetics of twin growth and its dependence on stress and temperature, one must first know the elementary behaviors of individual interfaces that build the twins, prior to studying their collective behavior. Naturally, the atomic structure of a given facet (i.e. coherent, semi-coherent, serrated…), its equilibrium and non-equilibrium defect content (dislocations, disconnections, faults…), and the interfacial excess energy will all play a role in its temperature-, and potentially stress-, dependent mobility. Such relationship between facet structure, migration mode and mobility is not known for all facets. Thus far, most attention has been placed on the CTB for which migration is mediated by the nucleation and propagation of disconnection loops/terraces [9,35–37]. Importantly, depending on stress and temperature, the kinetics of migrations are either limited by terrace nucleation or by propagation rates. Another critical point was recently raised in the case of the PB facet; its structure and consequently its mobility can drastically change depending on stress. Specifically, using MD simulations and HRTEM, the atomic-scale structures of BP facets in their unloaded / loaded states was characterized/simulated [28]. It was found using MD simulations that loaded BP serrated interfaces, which are composed of short coherent segments, relax into long coherent facets upon unloading. The resulting long facets are in good agreement with those observed in the microscope. Fully relaxed structures with misfit dislocations progressively form and eventually render the whole facet immobile. Conversely, upon subjecting this facet to a sufficiently large stress, MD simulations showed that these relaxed facets change back into a non-relaxed state and become mobile again [28]. Importantly, these results highlight that the level of stress relaxation of these interface structures have a strong effect on the corresponding stress and temperature dependent mobility. Currently, it is unclear whether these findings generally apply to all facets.

By only studying the intrinsic motion of facets one is unlikely to completely rationalize twin growth kinetics, at the very least during the early stages of growth of the twin embryo. First, the twin transformation will generate complex non-uniform stress/strain fields acting upon the twin facets [9–11]. The extent to which these internal stresses, which have been shown to be more intense along direction perpendicular to both the CTB boundary and shear direction, modulate the structure of facets is not clear. Second, to fully enclose the twin domain, facets will necessarily form junctions (e.g. PB facet connected to a CTB). Several studies [22,38,39] have focused on the structure of these junctions thereby proposing to mathematically represent them as disclinations. Importantly, in ref [39], atomistic simulations showed that the motion of these junctions is often accompanied by the emission of disconnections. This mechanism was then rationalized at the continuum level using a disclination dynamics framework which, in addition to postulating a crystallographic framework for disclination motion, showed that it is energetically favorable to emit a disconnection during the conservative non-planar motion of disclinations [40]. The overall role of this ‘coupled’ facet motion mediation by the emission of disconnections at facet junctions has not been quantified.

The aforementioned points suggest that both intrinsic facet motion and growth of 3D twin domains should be studied to rationalize the potential roles of both facet couplings and of internal stresses on twin growth. A first step was taken in this direction whereby combining MD and phase field modeling of a “crater” defect formed by inserting a dislocation shear loop onto a CTB [9]. It was found that facets such as the PB and Twist-PyPy1 migrate faster than other facets and that they control the kinetics of the crater. This result was attributed to the local stress field near facet junction and to the non-equilibrium structure and high mobility of these facets.

To more comprehensively address the aforementioned questions, we first report in this work MD simulations of model individual twin facets which were recently reported for $\{10\bar{1}2\}$ 3D twins in Mg [8]. New facets are also reported for a total of ten facets. The velocity of each facet is quantified as a function of the resolved shear stress (RSS) in the range 0–500 MPa, and temperatures in the range 100–500 K. Several facets are highly mobile and show a slight variation of velocity with changing stress and temperature. In contrast some interfaces, in particular the CTB and the BP/PB, show a strong dependence on stress and temperature. In light of the results mentioned above on the effect of stress relaxation on the structure and mobility of BP interfaces [28], we further quantify the relation between the mobility and the level of stress relaxation mediated by misfit dislocations as a function the applied stress and the temperature. Finally, to assess how the behavior of individual facets can change when connected together to build a 3D twin domain, the growth of a nanotwin is simulated for applied stresses in the range 1GPa-2 GPa for temperatures in the range 100 K-500 K. All this data is used and analyzed by means of an anisotropic phase field model recently developed [9]. First, we parameterize the phase field model with mobilities that depends on the type of facet (CTB, PB, Twist-PrPr2 etc.). The mobilities used in the PF model are calibrated from MD data for individual facets such that the facet velocity for a given RSS and temperature follows the values measured by MD simulations. With this phase field model, we simulate 3D twin growth by using the same initial twin embryo as in the MD simulations, for different stresses and temperatures. Among the different results presented, the simulations show importantly that the effective mobilities of some facets in a growing twin can be significantly different from those of individual facets. This is primarily attributed to the complex internal stress state of the twin, not limited to the RSS acting along the shear direction but also normal stresses and shear stresses in other directions. It can also be attributed to facet junctions which can alter facet migration mechanisms (i.e. constraint the state/configuration of a facet), and trigger coupled facet migration. As such, we propose then another version of the phase field model, whereby we fit directly both the twin growth kinetics and the twin shapes as predicted by MD so as to calibrate effective facets mobilities. Importantly, we also show that among the ten different facets initially considered, a limited set of rate-limiting facets can be identified, which controls the overall twin growth kinetics and morphology.

2. Molecular dynamics simulations

Given the large number of facets used in this study, Table 1 presents a list of all acronyms used in the rest of the study.

Table 1.
List of acronyms used throughout the manuscript.

Acronym	Definition
CTB	coherent twin boundary
FTB	front twin boundary
BP	basal - prismatic
PB	prismatic - basal
Tilt PyPy1	tilt pyramidal 1 - pyramidal 1
Twist PyPy1	twist pyramidal 1 - pyramidal 1
Twist PrPr2	twist prismatic 2 - prismatic 2
MD	molecular dynamics
PF	phase field
RSS	resolved shear stress
HRTEM	high resolution transmission electron microscopy
TD	twinning disconnection
BS	bright side
DS	dark side
K_1	normal direction
η_1	twinning direction
λ	transverse direction

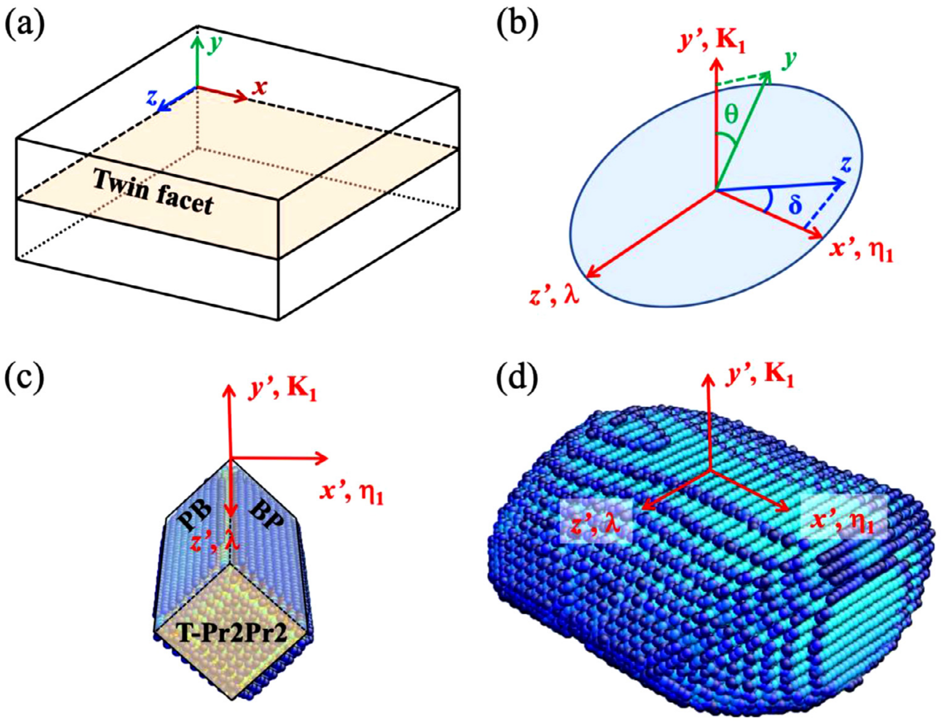

Fig. 1. (a) Schematics showing a bicrystal model containing a twin facet. (b) Two parameters δ and θ are used to define a twin facet. (c) An unrelaxed twin nucleus bound by BP, PB and T-PrPr2 interfaces. (d) Relaxed twin nucleus for loading.

2.1. Simulation setup

MD simulations are performed using LAMMPS [41]. The simulations employ the modified embedded atom method (MEAM) potential developed by Wu et al. [42].

2.1.1. Simulations of individual facets

Apart from the CTB, twin facets could adopt three configurations, (i) coherent, (ii) semi-coherent with partial stress relaxation and (iii) semi-coherent with fully relaxed stress, corresponding to different stages of twinning. At the beginning of the twin transformation, twins are enclosed by CTBs and short coherent twin facets. These can have large long-range stress and strain fields [5,28], resulting in a local deviation of orientation between twin and matrix from the perfect $(\bar{1}012)$ twin orientation [19,20,43]. As the twin grows, misfit dislocations can appear on these facets to relax the stress state, thereby destroying the local coherency on the facets. This process is mediated by dislocation rearrangement and/or emission of lattice dislocations [5,17,19,28]. The fully relaxed facet places the twin and matrix in the perfect/exact crystallographic $(\bar{1}012)$ twin orientation. The semi-coherent facets with stress partially relaxed is in the intermediate state. To first quantify the energy and mobility of twin facets, bicrystal models are used. To form CTB or semi-coherent facets with fully relaxed stresses, upper and lower crystals are created with perfect $(\bar{1}012)$ twin orientation. To form coherent facets without stress relaxation, a twin shear $s_0 = 0.13$ acting as a pre-strain is equally distributed to upper and lower crystals. When a lower pre-strain s is applied, semi-coherent facets with partially relaxed stresses are created. The ratio s/s_0 is used a simple metric for the degree of stress not relaxed. Further, the degree of stress relaxation can be estimated by $1 - s/s_0$.

The models which are schematically shown in Fig. 1(a), and have the following dimension $35 \times 20 \times 35\text{nm}^3$. In these models, the y-direction is normal to the twin facets, the z-direction is along the intersection line between the facet and twinning plane and the x-direction is along the cross-product of the y- and z-directions. Wang et al. [8] reported possible choices z-axis with relatively lower indexes. The alignment of a twin facet can be determined by two angles δ and θ. As shown in Fig. 1(b), δ is the angle between the z-axis and the twinning direction $\boldsymbol{\eta_1}$, and θ is the angle between the y-axis and the twin normal $\mathbf{K_1}$. The indices of all twin facets studied in this work as well as their δ and θ are shown in the **Appendix**. With periodic boundary conditions in x- and y-directions and a 1 nm fixed region adjacent to the surface normal to y-direction, the models are relaxed at 10 K until the maximum force on each atom is less than 5pN. The 1 nm fixed regions adjacent to the surface normal to the twin normal direction is applied because the periodic length in this direction is relatively large. To enable periodic boundary condition in the twin normal direction requires a much larger model and a longer computer time. The fixed boundary condition has negligible impact on the twin growth in this direction because TBs are always far from the fixed boundary. The interface energies of all relaxed facets considered in this work are then calculated and listed in Table 2. All facets are identified in the twin domain shown in Fig. 2. Note that the front twin boundary (FTB) and the coherent twin boundary (CTB) are conjugate boundaries. Hence, hereafter, all properties (energy, velocity, mobility) for the FTB are the same as for the CTB. At temperature ranging from 25 to 500 K, a stress tensor which produces a RSS associated with $(\bar{1}012)$ twinning (which could be 100, 300 and 500 MPa) is applied to the relaxed models to drive the migration of twin facets. The overall velocity of a facet is calculated by,

$$v = \frac{\dot{\varepsilon}_{xy'} L_y}{\varepsilon^{tw}_{xy'}} \tag{1}$$

where $\dot{\varepsilon}_{xy'}$ is the 12-component of the strain rate tensor defined in the coordinate in which the x'-axis is along the twinning direction $\boldsymbol{\eta_1}$, the y'-axis is along the twin normal direction $\mathbf{K_1}$, and the z'-

Table 2
Excess energies of twin facets and corresponding angles in the polar coordinate system.

Facet/Energy (J/m^2)		δ (°)				
		0 (BS)	38.8	49.9	67.2	90 (DS)
θ (°)	0	CTB/0.149	CTB/0.149	CTB/0.149	CTB/0.149	CTB/0.149
	37.9	–	–	B/0.130	–	–
	40.6	–	–	–	–	–
	45	BP/0.122	–	–	–	–
	49.8	–	–	–	–	Twist-PyPy1/0.112
	68.7	–	–	–	C/0.105	–
	75.3	–	–	–	–	–
	90	FTB/0.149	A/0.123	Tilt-PyPy1/0.112	D/0.092	Twist-PrPr2/0.096

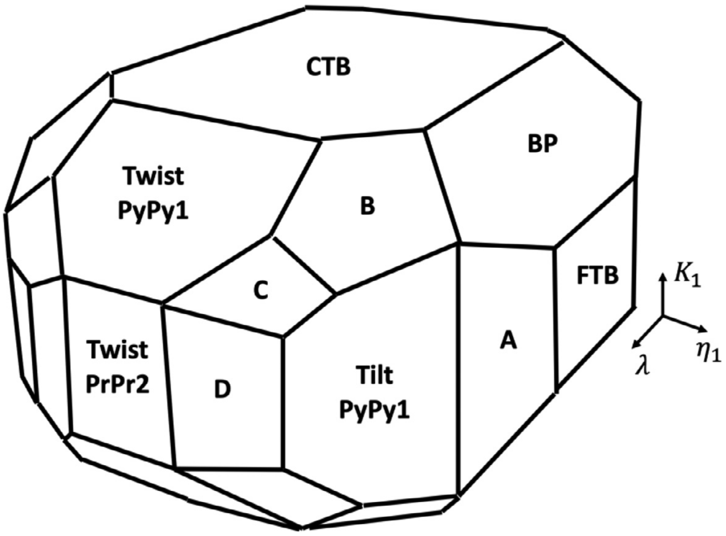

Fig. 2. Sketch of a three-dimensional twin showing all facets considered in the present work.

axis is along the zone axis $\boldsymbol{\lambda}$. L_y is the dimension of the model along the y-direction. $\varepsilon^{tw}_{xy'}$ is the 12-component of the characteristic strain associated with $(\bar{1}012)$ twinning, which is 0.065.

2.1.2. Simulations of three-dimensional twin growth

Construction of the model containing a 3D $(\bar{1}012)$ twin domain starts with a 60 × 30 × 60nm^3 single crystal in the coordinate system in which the x'-direction is aligned with the $[10\bar{1}1]$ direction, the y'-direction is normal to the $(\bar{1}012)$ plane and the z'-direction is along the $[1\bar{2}10]$ direction. Following the pure-shuffle mechanism associated with $(\bar{1}012)$ twinning [33], a 6 × 6 × 12nm^3 twin nucleus as shown in Fig. 1(c) which is bounded by coherent PB, BP and Twist-PrPr2 interfaces is created. With periodic boundary conditions in the x'- and z'-directions and a 1 nm fixed region adjacent to the surface normal to the y'-direction, the relaxed model as shown in Fig. 1(d) is obtained after multiple loading-unloading cycles under a deformation gradient with one non-zero simple shear component F_{12} at 5 K. With the same boundary conditions, a RSS which could be 1 or 2 GPa is imposed to the model at temperature 100 or 500 K to trigger growth of the twin domain. The dimensions of the twin domain along x'-, y'- and z'-directions are monitored during loading. Lastly, the MD simulations are stopped whenever one of the three dimensions of the 3D twin reaches half of the simulation box so that interaction between periodic images is weak.

2.2. Velocity of coherent facets at different temperatures and strain rates

Migration of coherent facets without stress relaxation is first investigated. Dang et al. [28] showed that the migrating twin facets are in non-relaxed states. Facets summarized in Table 1 are simulated. CTBs [29–31] and BP/PB facets [18,19,21,22,24,25,32–34] are widely reported. Twist-PyPy1 and Twist-PrPr2 facets on the lateral side of the twin are characterized [3,8,17,26,27]. In the most recent work, Tilt-PyPy1, C and D facets are observed via HRTEM. A and B facets are not reported yet but have relatively low indexes. Under loading producing 100, 300 or 500 MPa RSS at 25–500 K, we observe migration of most of the twin facets. Images of the onset of terrace nucleation which triggers migration of CTB ($\theta = 0°$), PB ($\delta = 0°$ and $\theta = 45°$) and Twist-PyPy1 ($\delta = 90°$ and $\theta = 49.8°$) interfaces are shown in Fig. 3. In Fig. 3(a), (c) and (e), terraces enclosed by the red dashed lines are disconnections on these facets. Migration of these facets is accomplished by nucleation and migration of these disconnection loops. This feature applies to all mobile facets tested in the simulations in this section. It is well accepted that motion of CTB along $\mathbf{K_1}$ direction (so-called twin growth) are accomplished by nucleation and migration of TDs on CTBs [9,35–37]. Twin propagation via other types of disconnections is unlikely. These results will be further compared with 3D simulations of twin propagation and growth in Section 2.3. Fig. 3(b), (d) and (f) shows the morphology of twin facets during migration. The CTB and Twist-PyPy1 interfaces remain flat during migration while the PB interface gradually shows a mountain-like morphology. The morphology is related to the relative nucleation rate and mobility of these disconnections.

Following Eq. (1), the average facet velocity is calculated. Fig. 4 shows the natural logarithm of facet velocity as a function of inverse temperature for facets with $\delta = 0°$ -these facets will be referred as bright side BS facets-. As shown, larger RSS are required at lower temperatures to move the facet. For all temperatures studied, the PB facet with $\theta = 45°$ shows higher velocity than the CTB

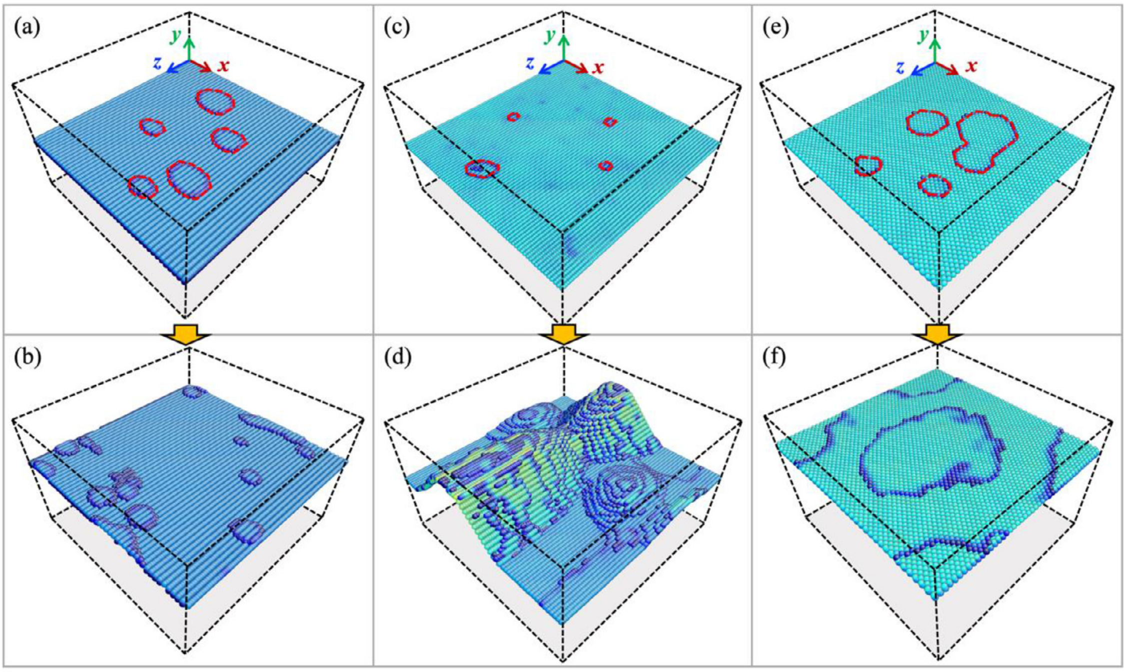

Fig. 3. Migration of a CTB under 300 MPa RSS at 200 K:(a) Nucleation of 2-layer TD loop on CTB. (b) CTB keeps flat during migration. Migration of a PB interface under 300 MPa RSS at 200 K: (c) Nucleation of 1-layer and 2-layer disconnection loop on PB interface. (d) PB interface shows mountain-like morphology during migration. Migration of a Twist-PyPy1 interface under 500 MPa RSS at 50 K: (e) Nucleation of 1-layer disconnection loop on Twist-PyPy1 interface. (f) Twist-PyPy1 interface keeps flat during migration.

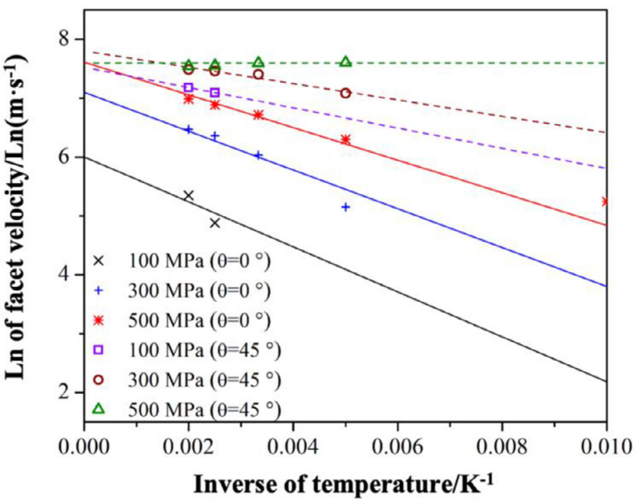

Fig. 4. Natural logarithm of average velocity as a function of inverse of temperature for the facets with $\delta = 0^\circ$. (Solid lines are associated with CTB with $\theta = 0^\circ$ and dashed lines are associated with PB with $\theta = 45^\circ$.).

with $\theta = 0^\circ$. A linear relation between natural logarithm of facet velocity and inverse of temperature is also found for both CTBs and PB facets. So, the facet velocity follows an Arrhenius-type law. Slopes associated with the PB facets with $\theta = 45^\circ$ are smaller than those associated with the CTBs with $\theta = 45^\circ$. For the same type of facet, the curve corresponding to a larger RSS shows a smaller slope, indicating that larger RSS minimize the effect of temperature likely as a result of the ease of terrace nucleation.

Fig. 5 plots the natural logarithm of facet velocity as a function of inverse of temperature for the facets with $\delta \neq 0^\circ$. These curves associated with $\delta \neq 0^\circ$ and $\theta \neq 0^\circ$ exhibit similar feature to each other. First, they can migrate at lower temperature and with smaller RSS compared to CTBs and PB facets. Second, their slopes are much smaller than the slopes associated with $\theta = 0^\circ$ as shown in Fig. 4, indicating that the migration of facets with $\delta \neq 0^\circ$ and $\theta \neq 0^\circ$ is less sensitive to temperature. That is likely due to a smaller terrace nucleation activation energy compared to the PB facet and CTB. Third, a close look at these curves shows that a linear relation stands at lower temperatures (~25–200 K) but fails at higher temperature (~300–500 K). In the range 300–500 K (as shown in the range 2.0×10^{-3}–3.3×10^{-3} inverse of temperature in the insets in Fig. 5), the facet velocity decreases when temperature increases. To rationalize these findings let us recall first that migration of facets is controlled by nucleation and further expansion of disconnections [35,36]. Depending on the facet type, stress and temperature, the rate limiting factor may be the nucleation of terraces or the propagation of nucleated loops. We note that the drop in velocity is only observed in facets which overall exhibit a minimal temperature dependence on mobility. Further, these facets tend to remain flat in all temperature regimes and also tend to move at high velocity. The drop is also found to be less important at higher temperatures. We speculate, that the velocity drop at high temperature is more likely to occur in facets with a low terrace nucleation barrier in which the propagation of terraces is rate limiting. In this case as temperature is increased thermal phonons are expected to limit the overall velocity of the facets. As stress is increased one can counterbalance the phonon drag; which rationalizes why this drop in velocities is less pronounced at higher stresses.

2.3. Reduction of facet velocity after stress relaxation

Stress relaxation of coherent facets is accompanied by formation of misfit dislocations which pin the motion of facets [17,28]. Here, we study the PB facets with different degree of stress relaxation. The estimation of the degree of stress relaxation is defined

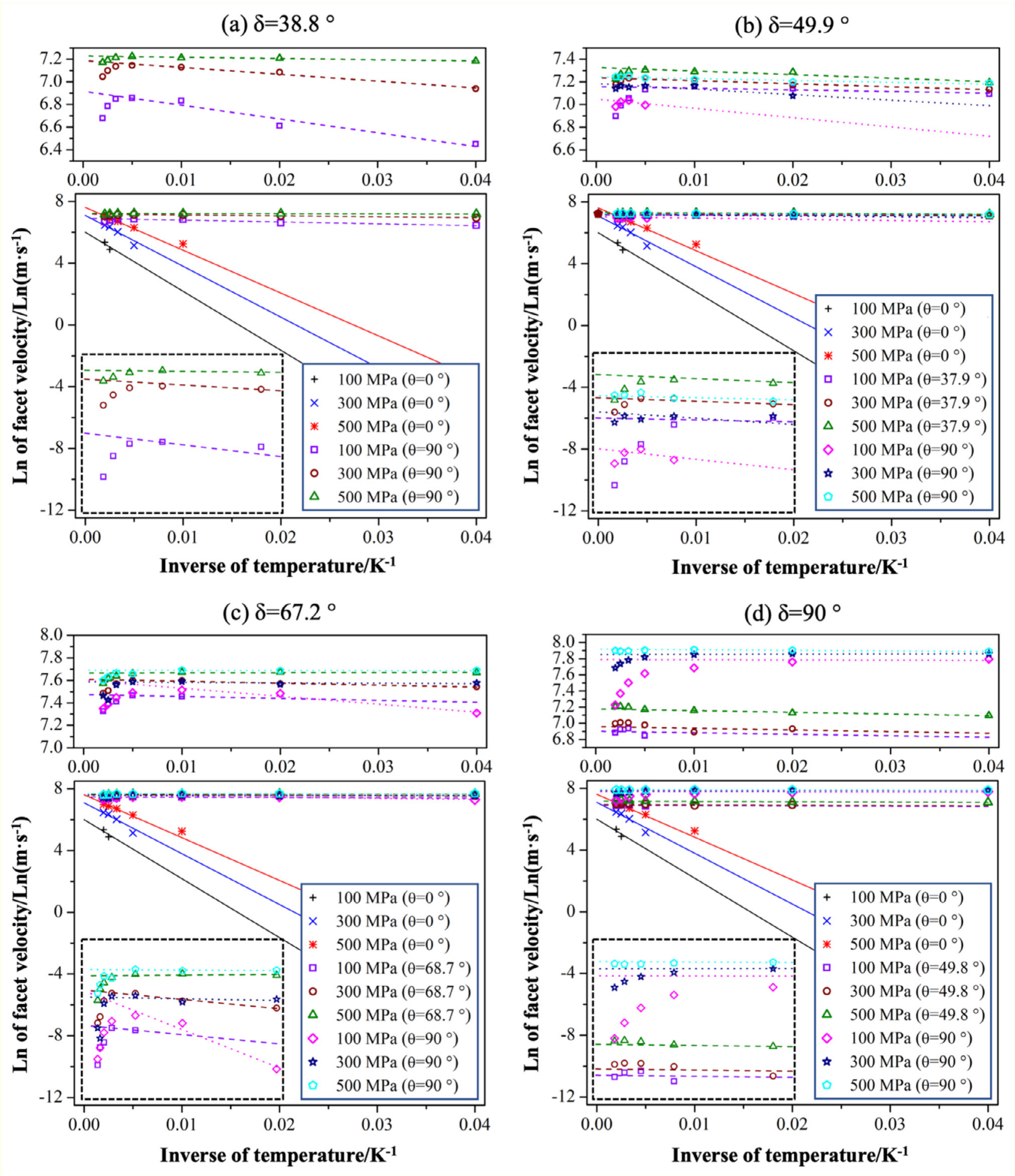

Fig. 5. Natural logarithm of average velocity as a function of inverse of temperature for the facets with (a) $\delta = 38.8^{\circ}$, (b) $\delta = 49.9^{\circ}$, (c) $\delta = 67.2^{\circ}$, and (d) $\delta = 90^{\circ}$. (The insets on the top show the curves in high velocity regime. The insets enclosed by dashed rectangles shows the curves in high temperature (100–500 K) regime.).

in Section 2.1. Fig. 6(a) and (b) demonstrates the effect of misfit dislocations which are marked by two yellow solid lines. As shown in Fig. 6(b), the coherent regions far from the misfit dislocations migrate faster than the other regions, showing obvious obstruction of the misfit dislocations to the motion of facets. Fig. 6(c) shows the shear strain associated with twinning as a function of loading time for the PB facets with different degree of stress relaxation under a loading that produces 300 MPa RSS at 200 K. Consistently with simulations from Dang et al. [28], the completely relaxed PB facet does not migrate. For the unrelaxed and partially relaxed PB facet, the shear strain rate (slope of curves in Fig. 6(c)) is relatively small at the beginning of loading. The shear strain rate increases with time because the stress field of nucleated terraces facilitates the nucleation of other terraces [35]. After some time, the shear strain rate reaches a constant value. Knowing the shear strain rate and following Eq. (1), velocities of PB facets are calculated. Corre-

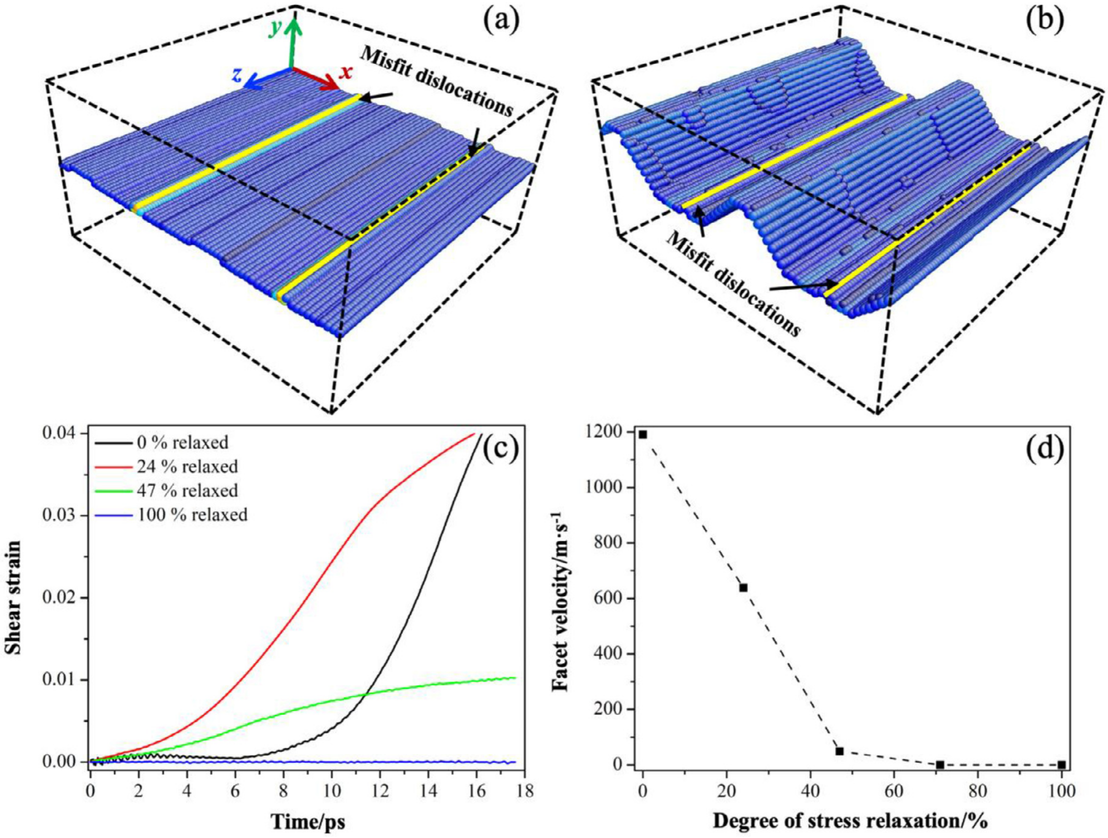

Fig. 6. (a) Initial configuration of a PB interface with two misfit dislocations. (b) Configuration after 18 ps loading producing 300 MPa RSS at 200 K. (c) Shear strain associated with twinning with respect to loading time. (d) Facet velocity with respect to degree of stress relaxation of the facet.

spondingly, the velocities increase with time and reach a steady value. These velocities are considered as the PB facet velocities and are plotted with respect to the amount of stress relaxation in Fig. 6(d). At the beginning of loading, the shear strain increases faster for the partially relaxed (24 and 47% relaxed) PB facets. This is probably because the local stress near misfit dislocation triggers the nucleation of disconnections while there is no preferred nucleation cite on unrelaxed (0% relaxed) PB facets. At later stages of loading, the disconnections continuously nucleate and the velocity reaches a steady value. As shown in Fig. 6(d), the average facet velocity decreases when the degree of stress relaxation increases. Clearly this simulation is not sufficient to demonstrate the effect of stress relaxation to all twin facets but shows a trend whereby the most relaxed facets have lower mobility.

2.3. Three-dimensional twin propagation and growth

By loading the initial configuration as shown in Fig. 1(d), the 3D twin may grow. It should be noted that a loading that produces at least 750 MPa is needed to avoid shrinkage of the twin (yet given the 3D nature of the twin domain and the anisotropy in facet mobilities, this imposed stress does not strictly stabilize the twin). We first examine the mechanisms associated with migration of twin facets. Taking the case (1 GPa RSS and 100 K) shown in Fig. 7(a) as an example, nucleation and migration of TDs on CTB and disconnections on BP/PB facet marked by the red dashed lines are observed. Meanwhile, no disconnection is found on the other facets. Migration of these facets is accomplished by motion of arrays of TDs instead of nucleation and migration of their own disconnections. Such observation is also found in the cases shown in Fig. 7(b)-(d). In these cases, migration of other facets is entirely coupled and driven by the nucleation of terraces (as single TD or array of TDs) at the junction between the CTB and PB facet. Fig. 7(c') shows the cross-section of the twin viewed along -$\boldsymbol{\lambda}$ direction containing the junction between CTB and PB facets. It shows a clear trend that TDs nucleate from the junction and glide towards the middle of CTB. However, cross-section viewed along $\boldsymbol{\eta_1}$ direction as shown in Fig. 7(c'') indicates that TDs nucleate far from the junction between CTB and facets on the lateral side of the twin. This is different from the mechanisms revealed in simulations in Section 2.2. The latter is likely more pertinent when the twin has grown to large sizes while the coupled migration process is expected to be more critical to the incipient growth of a twin embryo. We then examine the morphology of the 3D twins during loading. As shown in Fig. 7(a)-(d), the morphology of the twins varies when the RSS and the temperature change. Fig. 7(e) and (f) shows the change of dimensions in $\mathbf{K_1}$, $\boldsymbol{\eta_1}$ and $\boldsymbol{\lambda}$ directions with respect to loading time. The change of dimensions are fairly linear with loading time. Thus, the slopes represent the average velocity in different directions. At lower temperature (100 K) and with smaller RSS (1 GPa), twin growth in the $\boldsymbol{\lambda}$ direction is much faster than that in $\mathbf{K_1}$ and $\boldsymbol{\eta_1}$ directions, resulting in a strip-like twin as shown in Fig. 7(a). An increase in loading and temperature results in more isotropic twin growth. Fig. 7(e) compares the twin growth with the same loading (1 GPa) but at different temperatures (100 and 500 K). Changing the temperature from 100 to 500 K, the velocities along the $\mathbf{K_1}$, $\boldsymbol{\eta_1}$ and $\boldsymbol{\lambda}$ directions changes from 0 to 274 m/s, from 200 to 800 m/s and from 1540 to 1735 m/s. There is a dramatic increase in the velocity along $\mathbf{K_1}$ and $\boldsymbol{\eta_1}$ directions and a relatively small increase in the velocity along

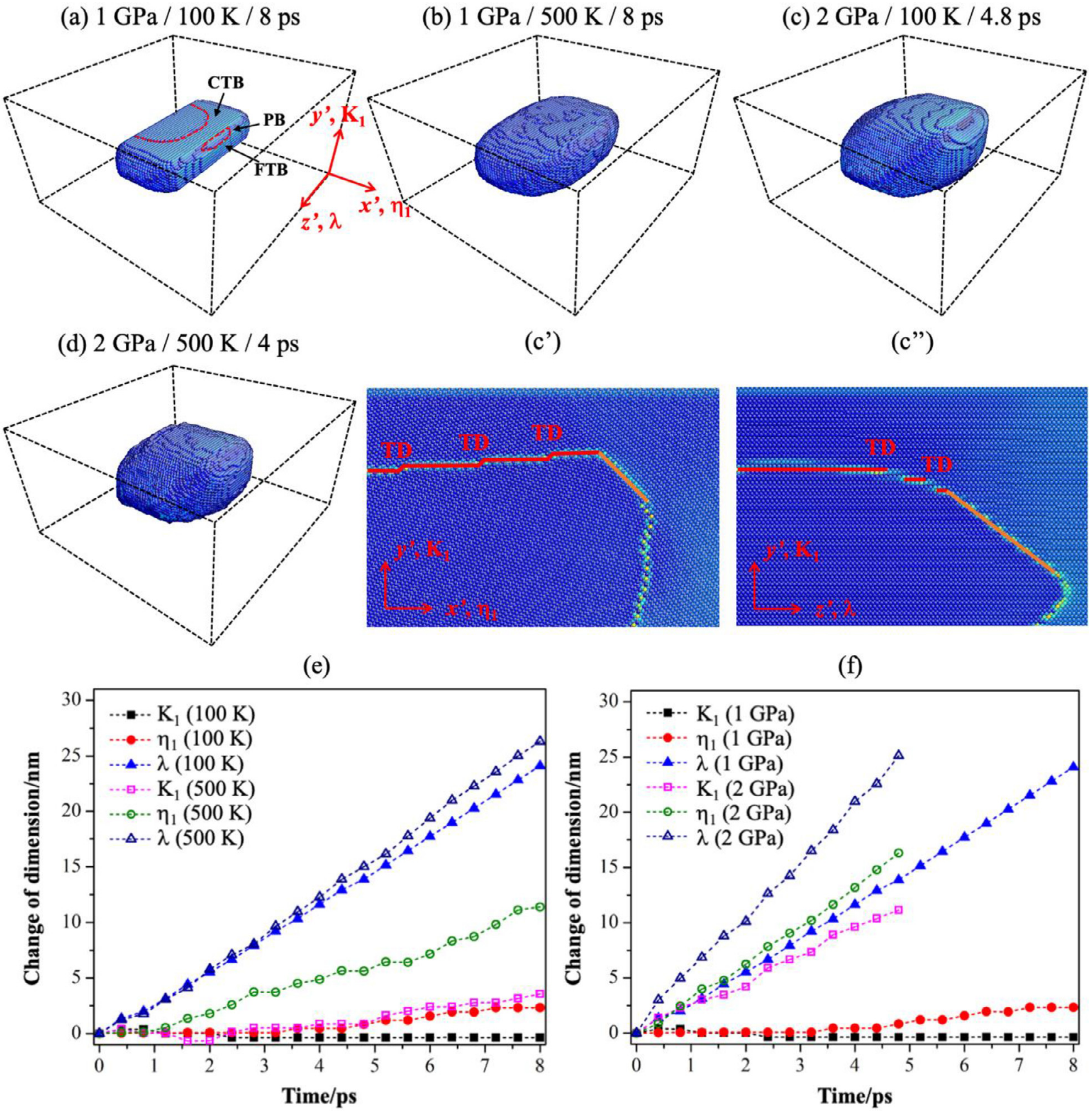

Fig. 7. Configuration of a 3D twin (a) after 8 ps loading producing 1 GPa RSS at 100 K, (b) after 8 ps loading producing 1 GPa RSS at 500 K, (c) after 4.8 ps loading producing 2 GPa RSS at 100 K, and (d) after 4 ps loading producing 2 GPa RSS at 500 K. The cross-section near the junctions between CTBs and twin facets viewed along (c') -$\boldsymbol{\lambda}$ direction and (c'') $\boldsymbol{\eta_1}$ direction(e) Change of dimensions of the 3D twin in $\mathbf{K_1}$, $\boldsymbol{\eta_1}$ and $\boldsymbol{\lambda}$ directions under a loading producing 1 GPa RSS at 100 and 500 K. (f) Change of dimensions of the 3D twin in $\mathbf{K_1}$, $\boldsymbol{\eta_1}$ and $\boldsymbol{\lambda}$ directions under a loading producing 1 and 2 GPa RSS at 100 K.

$\boldsymbol{\lambda}$ direction. Consequently, the twin shown in Fig. 7(b) shows more isotropic shape than the twin shown in Fig. 7(a). Twin growth and propagation along $\mathbf{K_1}$ and $\boldsymbol{\eta_1}$ directions is accomplished by nucleation and propagation of TDs on CTB and disconnections on BP/PB, which is temperature-dependent. Twin propagation along the $\boldsymbol{\lambda}$ direction is accomplished by migration of arrays of TDs, and is less temperature-dependent. Fig. 7(f) compares the twin growth with different loading magnitudes (1 and 2 GPa) but at the same temperature (100 K). Changing the RSS from 1 to 2 GPa, the velocities along the $\mathbf{K_1}$, $\boldsymbol{\eta_1}$ and $\boldsymbol{\lambda}$ directions changes from 0 to 1160 m/s, from 200 to 1695 m/s and from 1540 to 2519 m/s, resulting a twin morphology as shown in Fig. 7(c). Fig. 7(d) shows the twin morphology after 4 ps loading which produces 2 GPa RSS at 500 K. The changes of dimensions in $\mathbf{K_1}$, $\boldsymbol{\eta_1}$ and $\boldsymbol{\lambda}$ directions are 11.7, 13.6 and 19.6 nm. A particularly isotropic twin growth case is shown. The simulations of 3D twin propagation and growth reveal the twin growth along $\mathbf{K_1}$ direction mediated by TD on CTB, twin propagation along the $\boldsymbol{\eta_1}$ direction via disconnection on BP/PB facet and twin propagation along the $\boldsymbol{\lambda}$ direction via migration of arrays of TDs. The mechanisms associated with migration of facets with $\delta \neq 0^\circ$ and $\theta \neq 0^\circ$ revealed by simulation of single facet (in Section 2.2) and by 3D twin growth (in section 2.4) are different. This could be due to the aforementioned coupled migration process and to the significantly different stress profiles exerted on the facets in the 3D twin growth simulations vis a vis the individual facet migration simulations. However, some trends are similar in both cases. For example, both simulations reveal that the velocities of these facets with $\delta \neq 0^\circ$ and $\theta \neq 0^\circ$ are less temperature-dependent than the velocities of CTB and BP/PB facets.

For the sake of perspective, one should note that the 3D twin shapes predicted by MD simulations should be evidently different from the shape of twins in bulk polycrystalline hcp metals. Firstly, the size of simulation box (all dimensions less than 60 nm) and relaxation/loading time (less than 10 ps) are small. The 3D twin in MD simulations is much smaller in dimension than the twins in real cases. Meanwhile, defect content on twin facets is also different from that in real cases because the relaxation of stress associated with twin facets is assisted by thermal fluctuation and cannot be fulfilled in pico-second scale. In parallel, in MD simulations, the surroundings of the twins are defect-free, which differs from real cases in which twin growth is impeded by surrounding lattice dislocations, precipitates and grain boundaries. Misfit dislocations on twin facets, lattice dislocations and precipitates locally can pin the motion of twin facets, resulting in the irregular-shaped twins characterized in experiments [7].

3. Anisotropic phase-field model

Previously [9], we developed an anisotropic phase field model, whereby a facet dependent energy and mobility allowed deconvoluting the role of stress field and structure dependent energy and mobility on the kinetics of a “crater” defect formed on a CTB by MD simulations in Mg. Here, we further propose to use this model to reproduce and analyze the 3D twin growth morphology and kinetics as obtained by MD simulations presented above. As previously mentioned, we use a PF model with facet mobilities that depend on the type of facet (CTB, PB, Twist-PrPr2 etc.). The mobility values in the PF model are first calibrated from MD data for individual facets. More precisely, they are calibrated such that the facet velocity for a given RSS and temperature follows the values measured by MD simulations. We first use this model to simulate 3D twin growth for different stresses and temperatures, by using the same initial twin geometry as in MD simulations. A specific case, 100K-1 GPa, will be analyzed in detail in comparison with MD results. Second, we propose another strategy whereby we fit directly the effective mobilities from the twin growth kinetics and the twin shapes as predicted by MD simulations. In doing so, we can identify, among the ten facets initially considered, which are the rate-limiting facets that control the overall twin growth kinetics and morphology.

3.1. Phase field model

More details on the phase field model are available in [9]. The phase-field variable ϕ represents the local twin volume fraction at a material point. The matrix phase is $\phi = 0$ and the twin phase is $\phi = 1$. The continuous region where $0 < \phi < 1$ is the twin boundary. The Helmholtz free energy contains three contributions corresponding to the elastic strain energy E, the barrier energy f and the interfacial gradient energy Γ. Based on existing works [10,44–49], we write

$$F = \iiint_V (E + f + \Gamma) dV \tag{2}$$

The elastic strain energy density is

$$E = \frac{1}{2} \boldsymbol{\varepsilon^e} : \boldsymbol{C} : \boldsymbol{\varepsilon^e} \tag{3}$$

With

$$\boldsymbol{\varepsilon^e} = \boldsymbol{\varepsilon} - h(\phi) \boldsymbol{\varepsilon^{tw}} \tag{4}$$

$$\boldsymbol{C} = (1 - h(\phi)) \boldsymbol{C^M} + h(\phi) \boldsymbol{C^{tw}} \tag{5}$$

The stiffness tensors of the matrix and twin phase are $\boldsymbol{C^M}$ and $\boldsymbol{C^{tw}}$. The interpolation function is $h(\phi) = \phi^2(3 - 2\phi)$. ε is the total strain tensor and ε^{tw} is the strain due to twinning, with components $\varepsilon_{13}^{tw} = \varepsilon_{31}^{tw} = s_0/2$, $s_0 = 0.13$ is the twinning shear. The Cauchy stress tensor is

$$\begin{aligned} \boldsymbol{\sigma} = \boldsymbol{C} : \boldsymbol{\varepsilon^e} &= (1 - h(\phi)) \boldsymbol{C^M} : \left(\boldsymbol{\varepsilon} - h(\phi) \boldsymbol{\varepsilon^{tw}}\right) \\ &+ h(\phi) \boldsymbol{C^{tw}} : \left(\boldsymbol{\varepsilon} - h(\phi) \boldsymbol{\varepsilon^{tw}}\right) \end{aligned} \tag{6}$$

The barrier energy f is a double-well potential

$$f(\phi) = W \phi^2 (1 - \phi)^2 \tag{7}$$

where W is the height of the barrier equal to 7.5×10^8 J/m^3. The gradient energy Γ is

$$\Gamma = \frac{1}{2} \kappa |\nabla \phi|^2 \tag{8}$$

where ∇ is the Nabla operator. The coefficient κ includes dependence on $\nabla \phi$ to introduce an orientation dependent interfacial energy $\gamma(\nabla \phi)$ through

$$\kappa = \frac{18 \gamma^2}{W} \tag{9}$$

Note that Eq. (9) is a simplified expression exact for a one-dimensional interface when the elastic energy contribution to the total energy is neglected. We should keep in mind that in some critical cases (e.g. Twist-PrPr2 facet which can be subjected to large internal stresses), the elastic energy can contribute to the total energy by an amount as high as ~30%. The spatiotemporal evolution of the phase-field variable is given by

$$\frac{d\phi}{dt} = -L \frac{\partial F}{\partial \phi} \tag{10}$$

where L is the mobility. The energies of facets considered are shown in the table 1, while the corresponding facets are shown in the Fig. 2. All other facets have a higher energy (160mJ/m^2) so as to penalize their existence. Details on the implementation of facet dependent interfacial energy can be found in a recent work [9]. In a similar manner, we introduce a facet dependent mobility $L = L(\nabla \phi)$ discussed later on in this paper. We use general orthotropic elasticity for Mg, with $C_{11}=C_{22}=59{,}740$ MPa, $C_{33}=61{,}700$ MPa, $C_{12}=26{,}240$ MPa, $C_{13}=C_{23}=21{,}700$ MPa and $C_{44}=C_{55}=C_{66}=34{,}883$ MPa. $\boldsymbol{C^M}$and $\boldsymbol{C^{tw}}$ tensors are rotated according to parent and twin orientations with respect to the global axis system. The equations are numerically solved with a spectral code using Fast Fourier Transform (FFT) algorithms. The balance of Cauchy stress is solved with the accelerated scheme [50] with the use of the rotated scheme for the modified Green tensor [51] and of 1st/2nd order centered finite difference schemes for the calculation of all spatial derivatives [52]. The FFT grid is composed of 128 × 256 × 64 voxels in the twinning shear, transverse and normal directions, for all simulations. To ensure that no numerical pinning occurs, the voxel size is 0.431 nm in all directions. Twin growth is activated by applying a constant macroscopic shear stress Σ_{13} (creep) to the simulation box. In our simulations, the stress component σ_{13} corresponds to the RSS on the twin system. Fig. 8 shows a typical PF simulation of 3D twin growth, where facets are clearly visible. Their presence is due to the anisotropic mobility introduced in the PF model. Although the phase variable is a continuous function, as can be seen on the left figure, in the following we visualize discrete 3D twins using a threshold plot. As shown in the right figure (Fig. 8), we show only FFT voxels for which the phase field variable is greater or equal to 0.5. This plot allows for an easier comparison between PF and MD results.

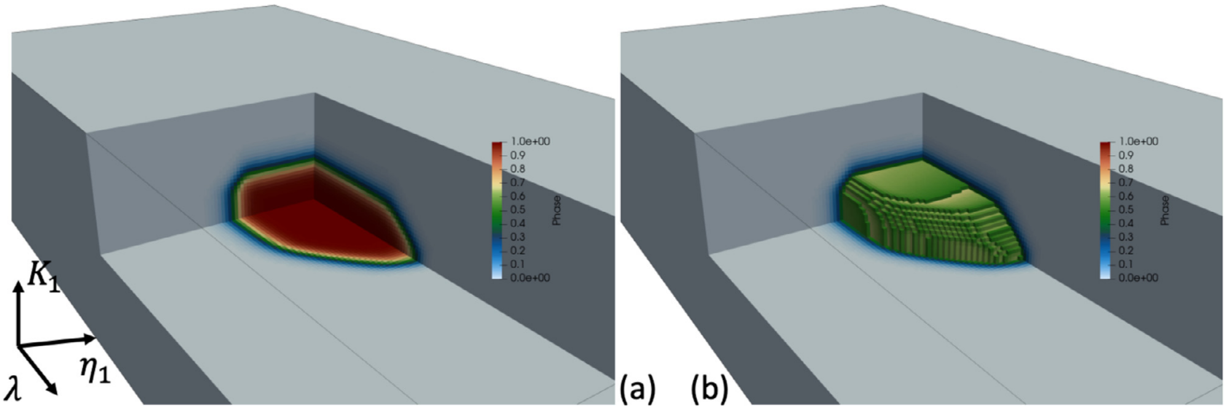

Fig. 8. Simulation of 3D twin growth with the PF model showing the presence of facets due to anisotropic mobility. (a) Phase field distribution. (b) Plot of the 3D twin obtained by showing all voxels where the phase field variable is greater or equal to 0.5.

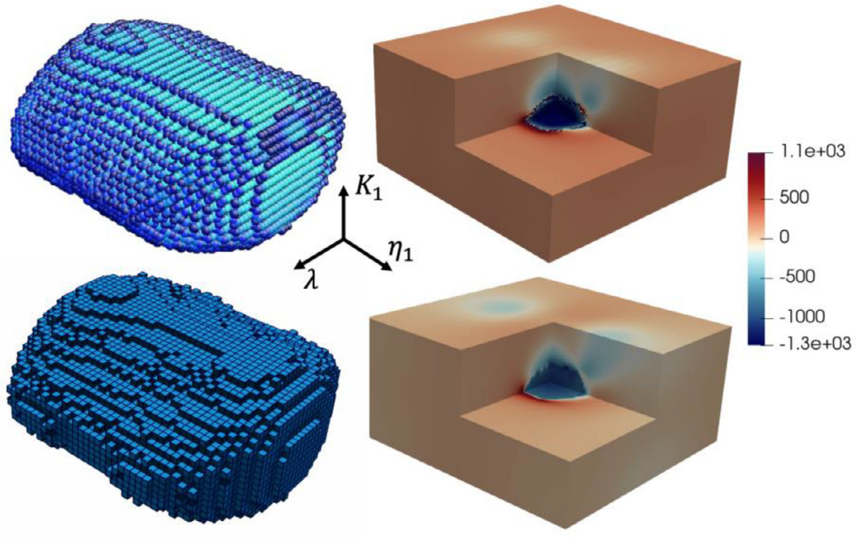

Fig. 9. Initial twin domain. Top: Initial twin and associated internal RSS field (MPa) in MD simulations. Bottom: Initial twin domain in the phase field simulations (threshold plot showing only $\phi > 0.5$) and associated internal RSS field (MPa), the color scale is the same for phase field and MD simulations.

3.2. *Initial twin domain*

The initial twin domain geometry in the phase field simulations is the same as that built from MD simulations. The size of the simulation box is ~55 nm, ~110 nm and ~28 nm in the shear, transverse and normal direction, respectively. In the same directions, the length of the initial twin is ~17 nm, ~19 nm and ~9 nm. The phase field variable is slightly smeared out in the twin boundary areas to set up diffuse interfaces that can move, such that PF simulations can start, and the twin can grow. This slight initial diffusion of the phase field can be seen in the profiles shown in the Fig. 9. The initial twin domain is shown in the Fig. 9, along with the distribution of the internal RSS. To yield direct comparison with MD results, the mean RSS value in the phase field model has been removed in the figure. The similarity between the stress fields obtained from MD and phase field models is appreciable. However, one must note that the negative stresses inside the twin are a much larger in MD simulations -the difference is up to 500 MPa in the middle of the twin, values are in better agreement across twin interfaces, MD stress magnitudes being still larger than PF values-. In the figure, strong positive stresses can be seen in the transverse direction in front of the twin boundary, while the upper and lower CTB interfaces are subjected to negative stresses. A closer inspection of stresses in the shear, transverse and normal directions is presented in the Fig. 10. In the transverse direction, the stresses acting on the Twist-PrPr2 interfaces are both positive and negative, positive values being slightly larger such that the mean RSS value across the Twist-PrPr2 facet is positive. Along the shear and normal directions however, the RSS acting on FTB and CTB facets is mostly negative, resulting in negative mean values across the facets. The mean RSS magnitude is larger for the CTB than for the FTB. As presented below, such stresses have a strong impact on the anisotropic twin growth kinetics.

3.3. *Simulation of twin growth with mobilities calibrated as per molecular dynamics simulations of individual facets*

In the phase field model, one can relate the mobility of an interface to its velocity and to the RSS applied on that interface. Such is done in phase field dislocation models and phase field twinning models [53]. Assuming a one-dimensional interface and that the elastic energy is negligible as compared to barrier and gradient energies (meaning that the diffuse interface is in equilibrium under the counteracting actions of driving forces coming from gradient

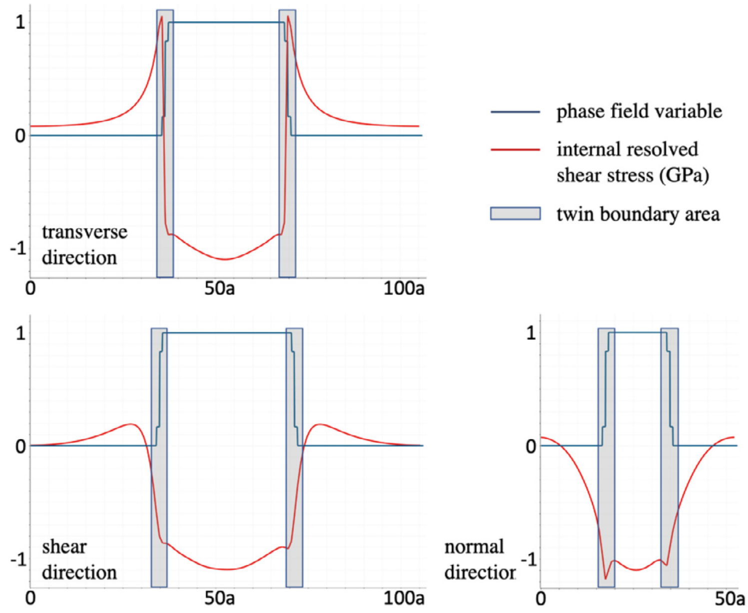

Fig. 10. Internal RSS profiles (GPa) in the initial twin domain in the phase field simulations (red lines). The phase field variable is plotted in dark blue lines. The gray shaded areas show Twist-PrPr2, FTB and CTB interfaces along the transverse, shear and normal directions, respectively. In the x axis, a denotes the lattice parameter in Mg, a = 0.321 nm. The mean stress value has been subtracted in the stress profiles. (For interpretation of the references to colour in this figure legend, the reader is referred to the web version of this article.)

and barrier energies), and assuming that the interface is moving in a stationary configuration (not deforming) at constant velocity v under the action of a RSS σ, one can write

$$L = \frac{v\sqrt{W}}{6\sqrt{2}\sigma\varepsilon\sqrt{\kappa}} \tag{11}$$

where L is the interface mobility and ε is the magnitude of the twin shear strain. In the forthcoming simulations, we use Eq. (11) to calibrate the mobility of facets in the PF simulations from the velocity curves obtained by MD simulations. The value σ corresponds to the mean RSS across the facets (it is processed during the PF simulation and updated at every timestep) in the PF simulations and v is the corresponding velocity measured in MD for a given RSS and temperature. Here as well, one should note that Eq. (11) is a simplification which (i) uses the gradient energy factor κ obtained from simplified Eq. (9) and, (ii) neglects the effect of internal stresses on interface mobility. It is difficult to evaluate how the internal stresses will affect the thickness and mobility of interfaces in a 3D growing twin. However, from the comparison of stress dependent facet velocities in the forthcoming PF simulations with MD simulations of individual facets, we observed that using Eqs. (9,11) give the expected trends for the growing twins. In situations where the mean RSS across facets exceeds the maximum value 500 MPa used in MD simulations of individual facets, linear extrapolation is used and we limit the maximum velocity to 3200 m/s, the order of the shear wave velocity in Mg.

It is important to note that for facets that are not reported in MD simulations (facets other than the ten reported facets in the Fig. 2 and Table 1), we chose to fix a larger mobility such that they do not appear during the PF simulations of twin growth. Indeed, using a smaller mobility for those facets leads to twin domains where only facets not desired are seen and the twin shape does not compare well with MD predictions. Conversely, with our choice, only reported facets appear in the PF simulations of twin growth, as the non-desired facets that form immediately disappear. Note also that for the FTB, we use both excess energy and mobility of the CTB.

Different results for the case (100 K-1 GPa) are presented in Fig. 11. We choose this case as the mean RSS across facets and the temperature are the lowest, such that it limits the effect of linear extrapolations made on the facet velocities. Fig. 11(a) shows the reference twin as obtained from MD simulations after 8 ps of loading. In the first phase-field simulation shown in Fig. 11b), we use all facet mobilities as estimated from MD data and Eq. (11). BP and PB facets are non-relaxed interfaces, hence very mobile. Although twin shape predicted by phase field shows features in good agreement with the MD result, we note some critical disagreement. BP and PB facets are not observed. This is because their mobility at ~700 MPa is too large, as we considered the mobility of non-relaxed facets. Also, Tilt-PyPy1 and B facets are too large (in particular the Tilt-PyPy1 facet), such that the twin shape is altered and becomes very sharp at the tip of the transverse side. This is because the mobility of these facets is too low. Concerning PB/BP facets, we run a new phase field simulation, whereby the mobility of BP and PB facets are calibrated by using velocities for 24% partially-relaxed facets obtained from MD simulations. In this case, the mobility of PB and BP facets is reduced, and they now can be barely seen in Fig. 11(c), in better agreement with MD simulations. Concerning Tilt-PyPy1 and B facets, we assume that Tilt-PyPy1 and B facets have an effective mobility that is greater than the mobility of individual facets. As such, we arbitrarily shift up their velocities by 800 m/s (increase the order of 50%). The result is shown in Fig. 10(d). The twin shape is now in better agreement with MD results. In particular, we can observe A, Tilt-PyPy1, B, C, D, Twist-PyPy1 and Twist-PrPr2 facets, which allow building the complex twin shape in front of the transverse direction. Finally, as we considered 24% relaxed BP and PB facets, it seems reasonable to increase the PB and BP excess energies in the PF simulations, as the facets contain misfit dislocations. We use the arbitrary value 0.3 J/m^2, instead of 0.122 J/m^2. The result is shown in Fig. 11(e). One can see that the BP and PB appear now more clearly (see white arrows in the figure) with better agreement with MD results.

Fig. 12 shows phase field predictions for the cases (500 K-1 GPa) and (100 K-2 GPa), which allows studying the effect of

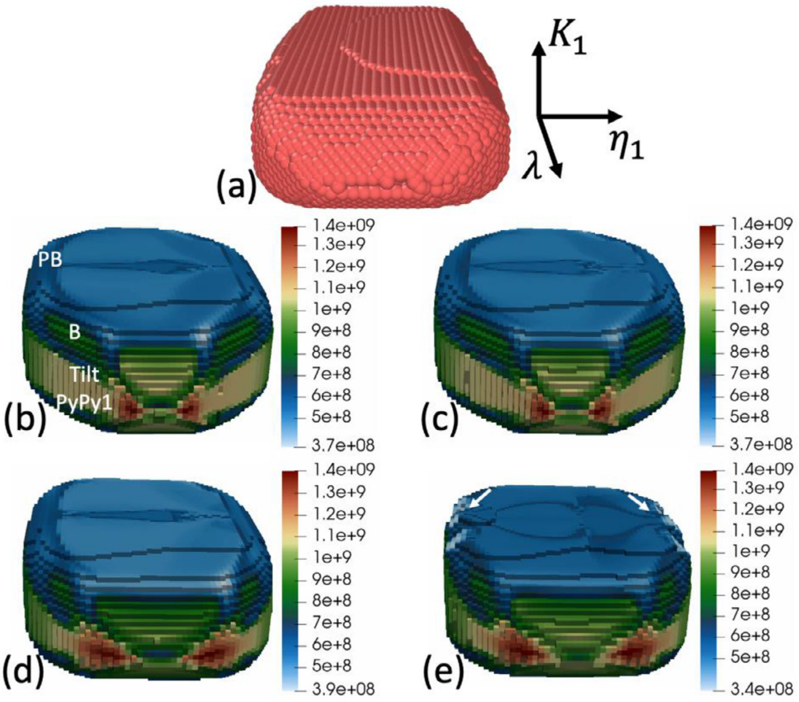

Fig. 11. Twin growth at 100 K and 1 GPa. (a) MD result. (b) Phase field result with facet mobilities calibrated as per MD simulations of individual facets. (c) Phase field result when using mobility of BP and PB calibrated from 24% relaxed facets from MD simulations. (d) Phase field result when correcting the mobility of Tilt-PyPy1 and B facets. (e) Phase field result when increasing the excess energy of 24% relaxed BP and PB facets. In (a, b, c, d), the mean stress across facets is shown with the color code (Pa).

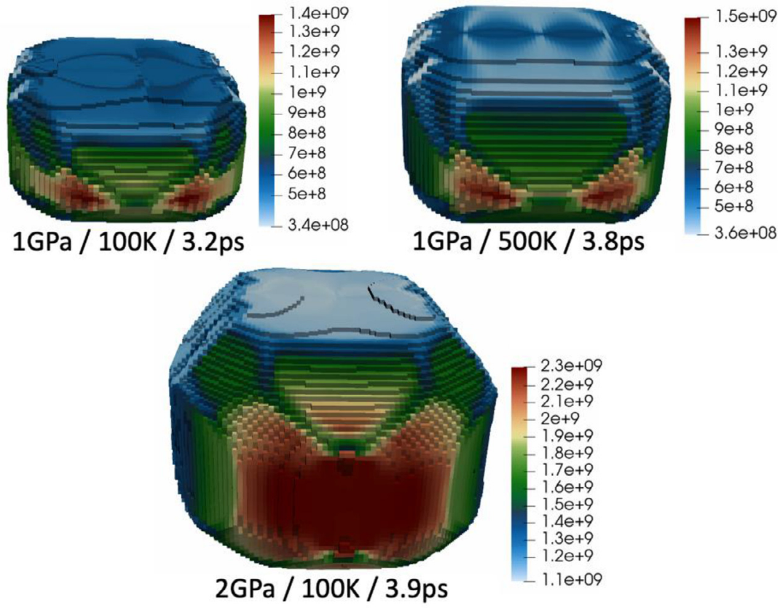

Fig. 12. Phase field results for different applied stresses and temperatures. Facet mobilities are calibrated from as per MD simulations of individual facets. BP and PB facets are 24% relaxed facets, with increased excess energy. Mobility of Tilt-PyPy1 and B facets are corrected. Color-coded is shown the mean stress across facets (Pa).

temperature or stress, as compared to the reference case (100 K, 1 GPa). Although we observe some resemblance with MD simulations, in particular the evolution of BP and PB facets (24% partially relaxed with increased energy), the twin shapes are in disagreement with MD results. In particular, while the propagation and shape of growing twins in the transverse direction appear to be relatively satisfactory, the coupled motion of FTB, PB/BP and CTB interfaces does not follow the kinetics predicted by MD.

The above results clearly indicate that the effective mobility of facets in a growing twin can be significantly different from the mobilities obtained when considering individual facets. In particular we found important changes for the Tilt-PyPy1, PB-BP, CTB and

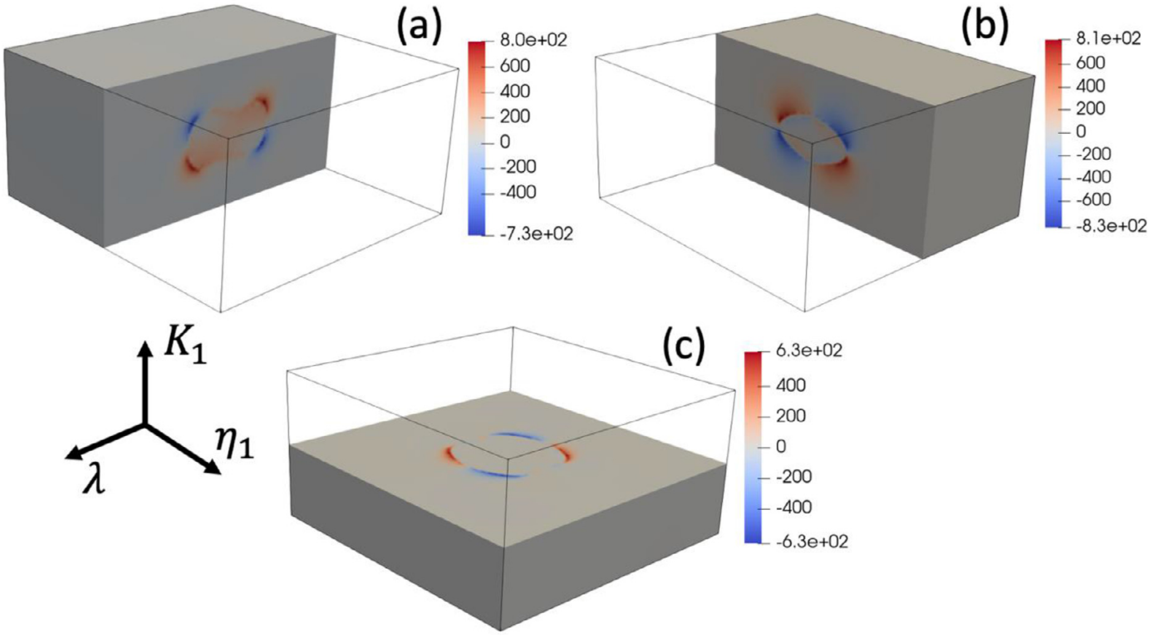

Fig. 13. Cuts revealing the complex three-dimensional internal stress state in the initial twin domain in the phase field model. (a) Internal normal stress $\sigma_{\eta 1 \eta 1}$ (Pa). (b) Internal shear stress $\sigma_{\lambda \eta 1}$ (Pa). (c) Internal shear stress $\sigma_{\lambda \kappa 1}$ (Pa).

FTB facets. It can be attributed to different factors. First, it is likely that junctions (in particular CTB-PB and FTB-PB junctions) trigger coupled motion of facets. Second, there exists a complex three-dimensional stress state in the twin domain, which certainly alters the twin facet motion. Third, this complex stress state could also condition which state (i.e. amount of relaxation) the facet finds itself in. In Figs. 10–12), we can see the remarkable differences in the RSS acting on the different twin facets. In Fig. 13, we further evidence the complex stress state by plotting other (normal and shear) components of the Cauchy stress tensor in different cuts. Facets can be subjected to very different stress states, importantly not limited to the macroscopically imposed RSS. Such stress field is clearly different from that in the MD simulations of individual facets. Note in particular in Fig. 13(a) that normal stress with alternating sign acting on the PB and BP facets. This might affect the mobility of the PB and BP facets and possibly explain the asymmetry in PB and BP facet sizes observed by MD in the Fig. 7.

3.4. *Phase field model with effective facet mobilities*

Taking into account the above results, we propose another strategy whereby we will calibrate effective mobilities of facets by directly fitting both the twin growth kinetics and morphology as predicted by MD simulations. More precisely, we will model the four cases shown in Fig. 7, namely (100 K-1 GPa), (100 K-2 GPa), (500 K-1 GPa) and (500 K-2 GPa). For each case, we assume that the facet mobility is constant and depends only on the type of facet. The facet mobilities are fitted until we can reproduce satisfactorily both the final twin shapes and the twin growth kinetics curves shown in the Fig. 7. The different mobilities obtained for the 4 cases will then be discussed with regards to MD data. As per the fitting procedure, we conclude that the most important, rate-limiting facets, which control both the twin morphology and the twin growth kinetics, are the CTB in the normal direction, PB/BP facets and the FTB along the shear direction, and Twist-PrPr2 and Twist-PyPy1 facets in the transverse directions. All other facets are found to be less important and they do not need to be used explicitly for calibration. We simply let these interfaces have a larger excess energy and mobility (energy is 0.161 J/m^2, effective drag in the Fig. 17 is ~2 × 10^{-4} Pa.s). The final twin shapes for the 4 cases tested are shown in the Fig. 14, where a reasonable agreement with MD is obtained.

The case (100 K-1 GPa) shown in Fig. 13(a) exhibits clearly a remarkable feature as compared to MD. Through a bulging mechanism, the PF model mimics the migration of the CTB by the nucleation and propagation of disconnection loops. The latter are nucleated at the junctions between BP/PB facets and CTB, and propagate along the CTB, making the latter migrating in the normal direction by elementary steps. One should keep in mind that these apparent discrete disconnection loops in Fig. 13(a) are not explicitly introduced in the PF model and that they result here from a threshold plot of the continuous phase field variable. However, like in MD, this mechanism predicted by PF, which actually mimics the nucleation and motion of not single disconnection loops but rather ensembles of disconnection loops given the PF spatial resolution, is driven by the internal shear stress field of the twin. In particular, the initiation of the bulging mechanism (disconnection loop nucleation) is caused by stress concentrations at the PB/CTB and BP/CTB junctions. The propagation is then driven by the applied stress.

In one applies a stress of 1 GPa but increases the temperature from 100 K to 500 K (compare Fig. 14(a) and (b)), the expansion of the twin along the shear direction is increased. Note that, in agreement with MD, the migration of the CTB remains mediated by this bulging mechanism initiating at the PB-CTB and BP-CTB junctions, whereas the FTB appears to migrate independently without assistance of PB/BP junctions. The RSS acting on the FTB is apparently sufficient to drive its motion, without requiring assistance of a bulging mechanism initiating at PB-FTB and BP-FTB junctions. Such is also observed for the motion of PB and BP facets, similarly to MD. At high stress and/or high temperature, Twist-PrPr2 facets are fast and barely visible, while the Twist-PyPy1 facets are present due to their lower mobility. Finally, Figs. 15 and 16 present the twin growth kinetics curves obtained by the simplified PF model. A very close agreement with MD results can be obtained. In par-

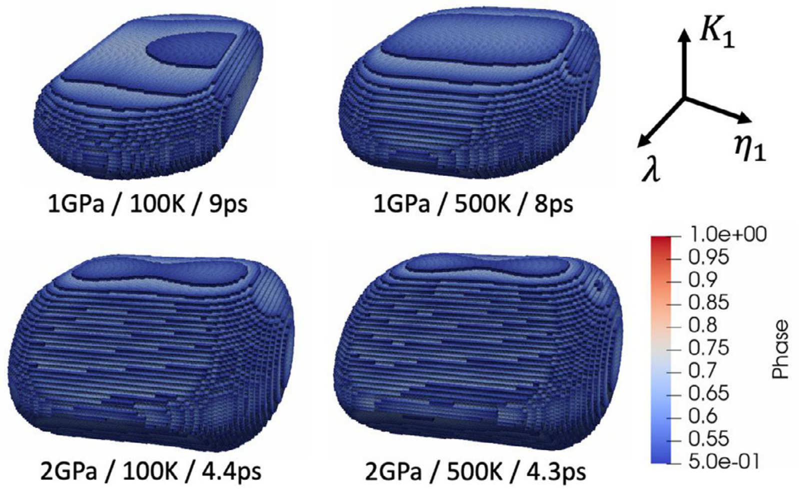

Fig. 14. Phase field simulations of twin growth at different applied stresses and temperatures (threshold plot showing only $\phi > 0.5$). The results should be compared with MD predictions in Fig. 6.

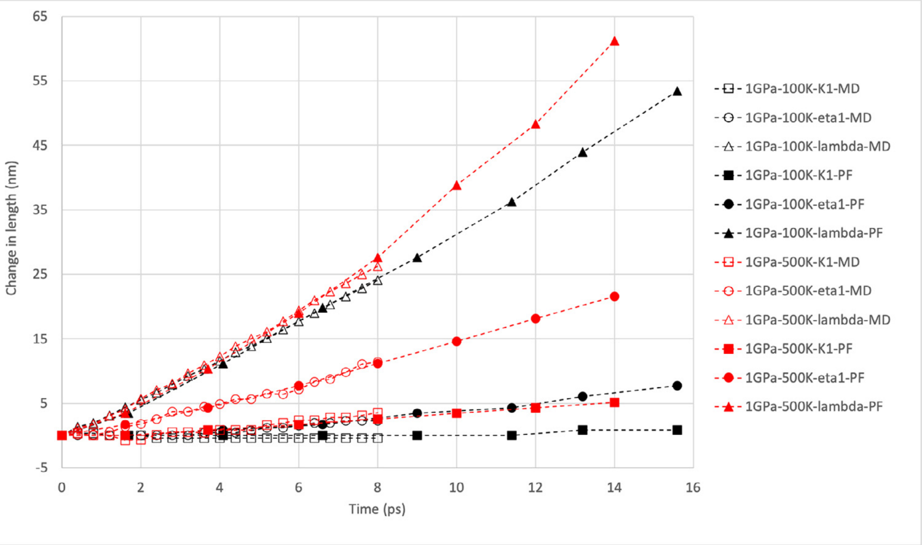

Fig. 15. Twin dimension evolution from the phase field simulations. Effect of temperature at 1 GPa. Similarly to Fig. 6, the curves show the changes of twin length in the shear (circles), transverse (triangles) and normal (squares) directions. MD values are also reported for comparison.

ticular, the PF simulations also predict a linear increase in the dimensions of the twin with time. A slight increase of rate in the transverse direction is observed for the cases at 100 K and can be attributed to periodic boundary conditions that cause an attractive effect of close opposite twin boundaries.

Fig. 17(a) shows the effective drag coefficients (inverse of effective mobility) found to match the MD predictions, in terms of 3D growth kinetics and final twin shapes. In this figure, interesting trends can be seen. First, we see that the CTB, FTB and PB facets exhibit a temperature dependence, in agreement with MD. This can be attributed to high activation energies and thermally activated migration mechanisms. Note that the mobility of the PB and BP facets should be low to see these facets in the twin. These low mobilities correspond to partially-relaxed facets, in agreement with Section 3.3. Second, as discussed, the mobility of the FTB should be larger than that of the CTB. This was attributed to both the effect of junctions with PB and BP facets and to the complex three-dimensional stress state of the twin. Last, all other facets show a limited temperature and stress dependence, suggesting lower activation energies for migration and in agreement with MD findings. The Twist-PrPr2 facet has the highest mobility and shows the smallest stress and temperature dependence.

In Fig 17(b) we now show a comparison of the effective drag coefficient obtained by fit of the PF model to the 3D twin growth kinetics predicted by MD (Section 3.4) vis a vis the drag coefficient obtained from Eq. (11) and MD simulations of individual facets (Section 3.3). One can see that overall, the effective drag for each facet is close but not exactly that of individual facets. The temperature dependence of CTB, FTB and PB/BP effective mobilities is naturally retrieved by the PF model. Significant differences between individual and connected facet mobilities are observed for the CTB and PB/BP facets. This observation is complementary to MD results, which showed that mobilities of individual and connected facets are different. Counterintuitively, we note that for the

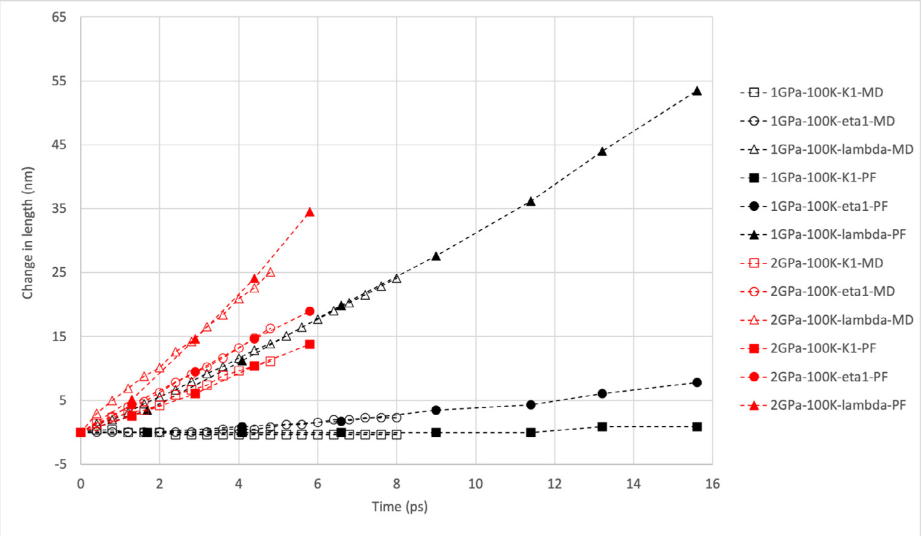

Fig. 16. Twin dimension evolution from the phase field simulations. Effect of stress at 100 K. Similarly to Fig. 6, the curves show the changes of twin length in the shear (circles), transverse (triangles) and normal (squares) directions. MD values are also reported for comparison.

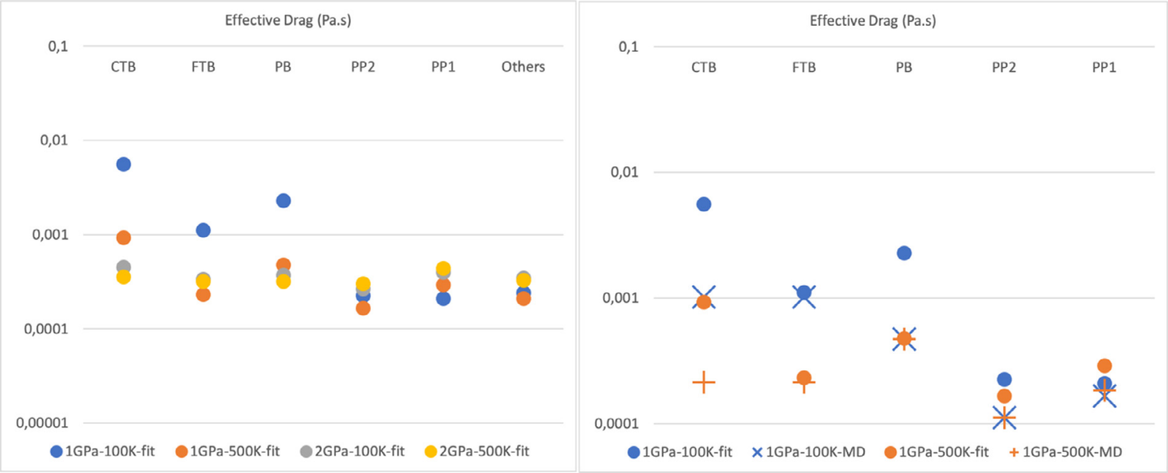

(a)

(b)

Fig. 17. (a) Effective drag of facets obtained by fit of MD simulations of 3D twin growth for the 4 cases considered. (b) Comparison of effective drag obtained by fit of 3D twin growth vs drag obtained from Eq. (11) and MD simulations of individual facets (cross symbols).

CTB and PB/BP facets, the effective drag is larger than that obtained using Eq. (11) together with the mean RSS across facets and MD velocities for individual facets. These differences could either be attributed to the coupled migration (i.e. bulging process) of the CTB and PB facets or to the fact that the presence of these junctions constrains the state of relaxation of the PB facets.

We conclude this section by further probing the relative importance of the internal RSS field and effective facet mobility on the twin growth morphology and kinetics, as a function of stress and temperature. To do so, we run another set of PF simulations presented in Fig. 18. We considered the cases (100K-1 GPa) and (500K-1 GPa) and tried PF simulations where we inverted the effective mobilities of the bright and dark sides. More precisely, the bright side facets (FTB, PB/BP) have the mobility of dark side facets (Twist-PrPr2, TwistPyPy1), and conversely. In this figure, simulations where the facet mobilities have not been swapped are on the left, while simulations with swapped mobilities are on the right. We considered only the cases for 1 GPa applied stress, because the cases with 2 GPa applied stress hinder the internal stresses values and their effects on twin growth. At low temperature (100 K), we observe strong effects when swapping the mobilities. It is then interesting to compare the propagation ratio 'transverse direction/shear direction' in the normal case to the ratio 'shear direction/transverse direction' in the swapped case. We should expect that they would be the same if the internal stress field of the twin had no influence on facet motion. Here however, the second ratio (i.e. shear/transverse) is lower than the first one, showing that the internal stress field plays an important role in the fast propagation in the transverse direction and the lower propagation in the shear direction. At 100 K, both the effective mobilities and the internal stress field are important. At 500 K however, one can see that the two ratios get appreciably closer, showing that the effect of internal stresses is predominant in twin growth.

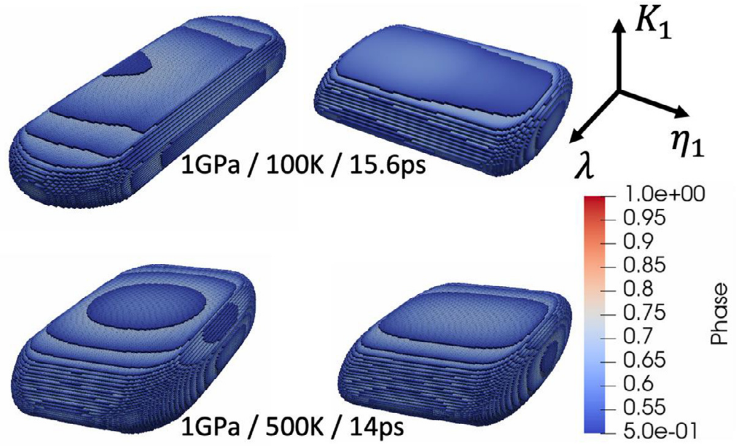

Fig. 18. Top: on the left, the twin shape after 15.6 ps at 1 GPa and 100 K predicted by PF using effective mobilities is shown. On the right is shown the twin shape when BS and DS mobilities are swapped. Bottom: on the left is shown the twin shape after 14 ps at 1 GPa and 500 K predicted by PF using effective mobilities. On the right is shown the twin shape when BS and DS mobilities are swapped.

4. Conclusions

This combined MD and PF study of individual facets and 3D twin growth considered the effect of facet structures, stress and temperature on the kinetics of relative facet migration rates and twin growth. The major results obtained are:

- A phase field model was derived and calibrated against atomistic simulations of planar facet motion and of growth of 3D twin domains. The phase field model is found to reproduce reasonably well the internal stress distribution surrounding the twin and as such provides acceptable estimates of the driving force for triggering the motion of facets. Through a bulging mechanism, the PF model is able to mimic the migration of the CTB by the nucleation of ensembles of disconnection loops at PB-CTB and BP-CTB junctions and their propagation along the CTB, although these crystal defects are not explicitly introduced in the PF model. The initiation of this bulging mechanism, like the nucleation of disconnections in the MD simulations, is driven by the local stress concentrations at the junctions.
- Some facets might change from a fully-relaxed, to a partially-relaxed structures under applied stress during twin growth, having a drastically different mobility and then affecting 3D twin growth. This was shown to be important for PB and BP facets, where using MD data for partially relaxed facets in the phase field simulations provides a better match of twin growth shapes and kinetics as compared to MD data. This result corroborates previous findings [28] and might be important for other facets.
- The mobility and relative contribution of individual facets on twin growth kinetics can change significantly when they are connected to other facets to build a 3D twin. This work reveals that the effective mobility of CTB, PB/BP facets can differ significantly from that extracted from the study of non-connected facets. This can be attributed to either coupled motion of facets or to the fact that junctions may prevent the PB/BP facet from fully relaxing.
- By running simulations where effective facet mobilities of bright and dark sides have been inverted, we found that at low temperature and low stress, both the heterogeneous internal stress field and effective facet mobilities are important to explain the anisotropy of twin growth. When increasing the temperature, the effect of internal stresses becomes predominant.
- As suggested by one of the PF model proposed, although many facets can be used to build a 3D twin, it appears that a limited set of rate-limiting facets controls the overall kinetics and morphology of twin growth. We found that these facets are the CTB in the normal direction, BP/PB facets and the FTB in the shear direction, and the Twist-PrPr2 and Twist-PyPy1 facets in the transverse directions.
- In the range of stress and temperature tested, it appears from both MD and phase field simulations that the mobility of most of interfaces show a slight dependence on stress and temperature, indicating low activation energies for their motion. This is not true however for the CTB, FTB and PB/BP interfaces, for which accounting for stress and temperature dependence is mandatory.

Declaration of Competing Interest

The authors declare that they have no known competing financial interests or personal relationships that could have appeared to influence the work reported in this paper.

Acknowledgements

This work was funded by the U.S. Dept. of Energy, Office of Basic Energy Sciences Project FWP 06SCPE401. V.T. would like to acknowledge the French Agence Nationale de la Recherche (ANR) through the program “Investment in the future” (LabEx “DAMAS” referenced as ANR-11-LABX-0008-01).

Appendix

Facet	δ (°) / θ (°)	**Index**
CTB	- / 0	$\{\bar{1}012\}\Vert\{10\bar{1}\bar{2}\}$
BP	0 / 45	$\{0002\}\Vert\{10\bar{1}0\}$
FTB	0 / 90	$\{10\bar{1}2\}\Vert\{\bar{1}01\bar{2}\}$
A	38.8 / 90	$\{14\bar{5}6\}\Vert\{14\bar{5}\bar{6}\}$
B	49.9 / 37.9	$\{\bar{1}\bar{1}21\}\Vert\{\bar{1}103\}$
Tilt-PyPy1	49.9 / 90	$\{0\bar{1}1\bar{1}\}\Vert\{01\bar{1}1\}$
C	67.2 / 68.7	$\{0\bar{1}10\}\Vert\{\bar{1}2\bar{1}2\}$
D	67.2 / 90	$\{1\bar{4}3\bar{2}\}\Vert\{\bar{1}4\bar{3}2\}$
Twist-PyPy1	90 / 49.8	$\{\bar{1}101\}\Vert\{0\bar{1}11\}$
Twist-PrPr2	90 / 90	$\{\bar{1}2\bar{1}0\}\Vert\{1\bar{2}10\}$

References

[1] J.W. Christian, S. Mahajan, Deformation twinning, Prog. Mater. Sci. 39 (1) (1995) 1–157.

[2] P.W. Bakarian, C.H. Mathewson, Slip and twinning in Magnesium single crystals at elevated temperatures, Trans. Metall. Soc. AIME 152 (1943) 226–254.

[3] Y. Liu, N. Li, S. Shao, M. Gong, J. Wang, R.J. McCabe, Y. Jiang, C.N. Tome, Characterizing the boundary lateral to the shear direction of deformation twins in magnesium, Nat. Commun. 7 (2016) 11577.

[4] Y. Liu, P. Tang, M. Gong, R. McCabe, J. Wang, C. Tomé, Three-dimensional character of the deformation twin in magnesium, Nat. Commun. 10 (1) (2019) 3308.

[5] M. Gong, G. Liu, J. Wang, L. Capolungo, C.N. Tomé, Atomistic simulations of interaction between basal <a>dislocations and three-dimensional twins in magnesium, Acta Mater. 155 (2018) 187–198.

[6] C.D. Barrett, H.El Kadiri, Impact of deformation faceting on {10-12}, {10-11} and {10-13} embryonic twin nucleation in hexagonal close-packed metals, Acta Mater. 70 (2014) 137–161.

[7] A. Fernández, A. Jérusalem, I. Gutiérrez-Urrutia, M. Pérez-Prado, Three-dimensional investigation of grain boundary–twin interactions in a Mg AZ31 alloy by electron backscatter diffraction and continuum modeling, Acta Mater. 61 (20) (2013) 7679–7692.

[8] S. Wang, M. Gong, R.J. McCabe, L. Capolungo, J. Wang, C.N. Tomé, Characteristic boundaries associated with three dimensional twins in hexagonal metals, Sci. Adv. In press. 2020.

[9] D.E. Spearot, V. Taupin, K. Dang, L. Capolungo, Structure and kinetics of three--dimensional defects on the {101¯2} twin boundary in magnesium: atomistic and phase-field simulations, Mech. Mater. (2020) 103314.

[10] P. Zhao, T.S.E. Low, Y. Wang, S.R. Niezgoda, Finite strain phase-field microelasticity theory for modeling microstructural evolution, Acta Mater. (2020).

[11] Y. Hu, V. Turlo, I.J. Beyerlein, S. Mahajan, E.J. Lavernia, J.M. Schoenung, T.J. Rupert, Disconnection-mediated twin embryo growth in Mg, Acta Mater. (2020).

[12] J. Wang, I.J. Beyerlein, J.P. Hirth, C.N. Tomé, Twinning dislocations on {-1011} and {-1013} planes in hexagonal close-packed crystals, Acta Mater. 59 (10) (2011) 3990–4001.

[13] Q. Yu, J. Wang, Y. Jiang, R.J. McCabe, N. Li, C.N. Tomé, Twin–twin interactions in magnesium, Acta Mater. 77 (2014) 28–42.

[14] C.N. Tomé, M.A. Kumar, J. Graham, K. Dang, Y. Liu, P. Tang, S. Wang, R.J. McCabe, L. Capolungo, in: Twin Transmission Across Grain Boundaries in Mg, Magnesium Technology 2020, Springer, 2020, pp. 3–5.

[15] M. Gharghouri, G. Weatherly, J. Embury, The interaction of twins and precipitates in a Mg-7.7 at.% Al alloy, Philos. Mag. A 78 (5) (1998) 1137–1149.

[16] J. Zhang, G. Xi, X. Wan, C. Fang, The dislocation-twin interaction and evolution of twin boundary in AZ31 Mg alloy, Acta Mater. 133 (2017) 208–216.

[17] M. Gong, J.P. Hirth, Y. Liu, Y. Shen, J. Wang, Interface structures and twinning mechanisms of twins in hexagonal metals, Mater. Res. Lett. (2017) 1–16.

[18] X.Y. Zhang, B. Li, X.L. Wu, Y.T. Zhu, Q. Ma, Q. Liu, P.T. Wang, M.F. Horstemeyer, Twin boundaries showing very large deviations from the twinning plane, Scr. Mater. 67 (10) (2012) 862–865.

[19] B. Xu, L. Capolungo, D. Rodney, On the importance of prismatic/basal interfaces in the growth of twins in hexagonal close packed crystals, Scr. Mater. 68 (11) (2013) 901–904.

[20] J.P. Hirth, J. Wang, C.N. Tomé, Disconnections and other defects associated with twin interfaces, Prog. Mater. Sci. 83 (2016) 417–471.

[21] A. Ostapovets, R. Gröger, Twinning disconnections and basal–prismatic twin boundary in magnesium, Model. Simul. Mater. Sci. Eng. 22 (2) (2014).

[22] J. Wang, L. Liu, C.N. Tomé, S.X. Mao, S.K. Gong, Twinning and de-twinning via glide and climb of twinning dislocations along serrated coherent twin boundaries in hexagonal-close-packed metals, Mater. Res. Lett. 1 (2) (2013) 81–88.

[23] Q. Zu, X.-Z. Tang, S. Xu, Y.-F. Guo, Atomistic study of nucleation and migration of the basal/prismatic interfaces in Mg single crystals, Acta Mater. 130 (2017) 310–318.

[24] B.-Y. Liu, L. Wan, J. Wang, E. Ma, Z.-W. Shan, Terrace-like morphology of the boundary created through basal-prismatic transformation in magnesium, Scr. Mater. 100 (2015) 86–89.

[25] B.-Y. Liu, J. Wang, B. Li, L. Lu, X.Y. Zhang, Z.-W. Shan, J. Li, C.-L. Jia, J. Shu, E. Ma, Twinning-like lattice reorientation without a crystallographic twinning plane, Nat. Commun. 5 (2014).

[26] M. Gong, S. Xu, L. Capolungo, C.N. Tomé, J. Wang, Interactions between< a>dislocations and three-dimensional {112¯ 2} twin in Ti, Acta Mater. (2020).

[27] X.-Z. Tang, Q. Zu, Y.-F. Guo, The surface nucleation of tension twin via pure-shuffle mechanism: the energy landscape sampling and dynamic simulations, J. Appl. Phys. 123 (20) (2018) 205112.

[28] K. Dang, S. Wang, M. Gong, R.J. McCabe, J. Wang, L. Capolungo, Formation and stability of long basal-prismatic facets in Mg, Acta Mater. 185 (2020) 119–128.

[29] A. Serra, D.J. Bacon, R.C. Pond, Dislocations in interfaces in the hcp metals—I. Defects formed by absorption of crystal dislocations, Acta Mater. 47 (5) (1999) 1425–1439.

[30] Y. Wang, L.Q. Chen, Z.K. Liu, S.N. Mathaudhu, First-principles calculations of twin-boundary and stacking-fault energies in magnesium, Scr Mater. 62 (9) (2010) 646–649.

[31] Z. Pei, X. Zhang, T. Hickel, M. Friák, S. Sandlöbes, B. Dutta, J. Neugebauer, Atomic structures of twin boundaries in hexagonal close-packed metallic crystals with particular focus on Mg, NPJ Comput. Mater. 3 (1) (2017) 1–7.

[32] Q. Sun, X.Y. Zhang, Y. Ren, J. Tu, Q. Liu, Interfacial structure of {10-12} twin tip in deformed magnesium alloy, Scr. Mater. 90–91 (2014) 41–44.

[33] J. Wang, S.K. Yadav, J.P. Hirth, C.N. Tomé, I.J. Beyerlein, Pure-shuffle nucleation of deformation twins in hexagonal-close-packed metals, Mater. Res. Lett. 1 (3) (2013) 126–132.

[34] C.D. Barrett, H.El Kadiri, The roles of grain boundary dislocations and disclinations in the nucleation of {10-12} twinning, Acta Mater. 63 (2014) 1–15.

[35] D.E. Spearot, L. Capolungo, C.N. Tomé, Shear-driven motion of Mg {10 1¯ 2} twin boundaries via disconnection terrace nucleation, growth, and coalescence, Phys. Rev. Mater. 3 (5) (2019) 053606.

[36] A. Luque, M. Ghazisaeidi, W.A. Curtin, A new mechanism for twin growth in Mg alloys, Acta Mater. 81 (2014) 442–456.

[37] A. Serra, R.C. Pond, D.J. Bacon, Computer simulation of the structure and mobility of twinning disclocations in hcp metals, Acta Metall. Mater. 39 (7) (1991) 1469–1480.

[38] J. Tu, X. Zhang, J. Wang, Q. Sun, Q. Liu, C.N. Tomé, Structural characterization of {10-12} twin boundaries in cobalt, Appl. Phys. Lett. 103 (5) (2013) 051903.

[39] A. Ostapovets, A. Serra, Characterization of the matrix–twin interface of a (101^{2}) twin during growth, Philos. Mag. 94 (25) (2014) 2827–2839.

[40] L. Capolungo, V. Taupin, GD 3: generalized discrete defect dynamics, Mater. Theory 3 (1) (2019) 2.

[41] S. Plimpton, Fast parallel algorithms for short-range molecular dynamics, J. Comput. Phys. 117 (1) (1995) 1–19.

[42] Z. Wu, M.F. Francis, W.A. Curtin, Magnesium interatomic potential for simulating plasticity and fracture phenomena, Model. Simul. Mater. Sci. Eng. 23 (1) (2015).

[43] A. Ostapovets, J. Buršík, R. Gröger, Deformation due to migration of faceted twin boundaries in magnesium and cobalt, Philos. Mag. 95 (36) (2015) 4106–4117.

[44] J.D. Clayton, J. Knap, A phase field model of deformation twinning: nonlinear theory and numerical simulations, Physica D 240 (9–10) (2011) 841–858.

[45] T.W. Heo, Y. Wang, S. Bhattacharya, X. Sun, S. Hu, L.-Q. Chen, A phase-field model for deformation twinning, Philos. Mag. Lett. 91 (2) (2011) 110–121.

[46] S.M. Allen, J.W. Cahn, A microscopic theory for antiphase boundary motion and its application to antiphase domain coarsening, Acta Metall. 27 (6) (1979) 1085–1095.

[47] L.-Q. Chen, Phase-field models for microstructure evolution, Annu Rev. Mater. Res. 32 (1) (2002) 113–140.

[48] Y. Gu, L.-Q. Chen, T.W. Heo, L. Sandoval, J. Belak, Phase field model of deformation twinning in tantalum: parameterization via molecular dynamics, Scr. Mater. 68 (7) (2013) 451–454.

[49] J.J. Eggleston, G.B. McFadden, P.W. Voorhees, A phase-field model for highly anisotropic interfacial energy, Physica D 150 (1–2) (2001) 91–103.

[50] H. Moulinec, P. Suquet, A computational scheme for linear and nonlinear composites with arbitrary phase contrasts, Int. J. Numer. Methods Engrg. 52 (2001) 139–160.

[51] F. Willot, Fourier-based schemes for computing the mechanical response of composites with accurate local fields, Comptes Rendus Mécanique 343 (3) (2015) 232–245.

[52] S. Berbenni, V. Taupin, C. Fressengeas, L. Capolungo, A Fast Fourier Transform-based approach for generalized disclination mechanics within a couple stress theory, in: Generalized Continua as Models for Classical and Advanced Materials, Springer, 2016, pp. 47–75.

[53] A. Ruffini, Y.Le Bouar, A. Finel, Three-dimensional phase-field model of dislocations for a heterogeneous face-centered cubic crystal, J. Mech. Phys. Solids 105 (2017) 95–115.